Available online at www.sciencedirect.com
SCIENCE DIRECT®
Journal of Crystal Growth 271 (2004) 128–133
JOURNAL OF CRYSTAL GROWTH
www.elsevier.com/locate/jcrysgro

Growth of strontium barium niobate: the liquidus–solidus phase diagram

Michael Ulex, Rainer Pankrath, Klaus Betzler*

Fachbereich Physik, Universität Osnabrück, Barbarastr. 7, D-49069 Osnabrück, Germany

Received 1 July 2004; accepted 16 July 2004
Communicated by M. Roth
Available online 11 September 2004

Abstract

The liquidus–solidus phase diagram of strontium barium niobate, $Sr_xBa_{1-x}Nb_2O_6$, is determined over the whole existence region of the tetragonal phase. For this purpose, single crystals of various compositions within this range were grown. The compositions of the melts and the grown crystals as well as the corresponding liquidus temperatures were accurately determined. The tetragonal phase was found to exist from a lower limit with the crystal composition $x = 0.26$ to an upper limit of $x = 0.87$. The respective liquidus temperatures vary between 1452 and 1492 °C.

PACS: 42.70.Mp; 77.84.Dy; 81.10.Fq

Keywords: A1. Phase diagrams; A2. Czochralski method; A2. Growth from the melt; A2. Single crystal growth; B1. Niobates; B2. Ferroelectric materials

1. Introduction

Due to its outstanding photorefractive, electro-optic, nonlinear optic, and dielectric properties, strontium barium niobate, $Sr_xBa_{1-x}Nb_2O_6$—henceforth denoted as SBN, is one of the most interesting materials in these fields. Potential applications include pyroelectric detection [1], holographic data storage [2], surface acoustic wave devices [3], phase conjugation [4], generation of photorefractive solitons [5], quasi-phase-matched second-harmonic generation [6], and electro-optic modulation [7].

SBN crystallizes in a tetragonal tungsten bronze structure over a wide solid solution range. During the first investigations on SBN [1,8–11], a phase diagram was established [12] with a congruently melting composition at $x = 0.5$. Later, more specialized investigations [13] determined this congruently melting composition to $x = 0.61$. As

*Corresponding author. Tel.: +49-541-969-2636; fax: +49-541-969-12636.
E-mail address: Klaus.Betzler@uos.de (K. Betzler).

0022-0248/$ - see front matter © 2004 Elsevier B.V. All rights reserved.
doi:10.1016/j.jcrysgro.2004.07.039

crystal growth at such a composition is greatly facilitated, practically all publications up to now deal with properties of SBN with $x = 0.61$. Due to the different ionic sizes of strontium and barium, however, which give rise to different preferred sites in the unfilled tungsten bronze structure [10,14], all physical properties of SBN are composition dependent. The properties of SBN thus could be tailored in a certain range choosing an appropriate composition.

For a reliable growth of SBN at compositions other than the congruently melting one, yet, accurate knowledge about the liquidus–solidus phase diagram is indispensable. To achieve this, we have grown SBN samples with crystal compositions from $x = 0.32$ to 0.82 with steps of about $\Delta x = 0.05$.

2. Crystal growth technique

The crystals were grown by the Czochralski technique. Fig. 1 shows the set-up used. The melt is heated by four u-shaped resistance heating elements. The vertical temperature gradient in the furnace is about 1 °C/cm. An additional heater can be used to reduce the temperature gradient further. The temperature is measured by several thermocouples near the heaters, using a computer-based controller a temperature stability of better than ±0.1 °C is achieved. The platinum crucible with the melt is supported by a ceramic rod, which is connected to a balance. The seed crystal is fixed to an air cooled ceramic rod rotating with 28 cycles per minute. The crystal grows in *c*-direction and is pulled out with a speed of 0.4–0.8 mm/h. The computer, which monitors the balance, regulates the temperature such that a growth with constant crystal diameter (≈ 5 mm) is accomplished.

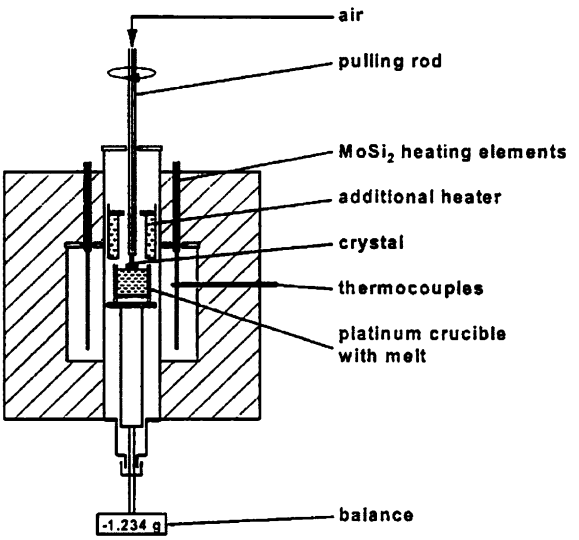

Fig. 1. Crystal growth apparatus.

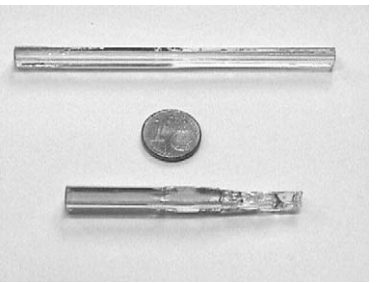

Fig. 2. Czochralski-grown strontium barium niobate crystals.

For each of the compositions, the growth was started with a melt of initial weight of approximately 115 g. As seed crystals, samples of crystals with nearby compositions were used (difference in x less than 0.06). It turned out that at compositions above $x = 0.5$ the growth was rather insensitive to small temperature fluctuations. Thus in this region, comparably large crystals up to a length of 90 mm could be grown, corresponding to a weight of approximately 12 g. The sensitivity to fluctuations increases to lower x, the strontium-poor side, especially in the range $x < 0.35$ where only smaller crystals up to a length of 35 mm could be grown. Typical crystals, grown in that way, are shown in Fig. 2.

3. Determination of the composition

For the determination of the liquidus–solidus phase diagram, the liquidus temperatures (discussed in the next section) and the compositions of both, melts and corresponding crystals, have to be accurately known. While the melt composition is given by the initial weights, the accurate

determination of the crystal composition is a more complicated task.

To solve it, we used wavelength-dispersive X-ray fluorescence analysis (Siemens SRS analyzer). The X-ray source, a tube with chromium anode, was driven at 50 kV and 40 mA. As a measure for the strontium and barium contents, the characteristic fluorescence lines strontium Kα and barium Lα were chosen. For the wavelength dispersion a LiF analyzer crystal was used.

For the measurements, tablet-shaped samples with a thickness of 5 mm and a diameter of 30 mm were made from a solution of 10% crystal material in Spectromelt® A12 (Lithium Borate glass). To obtain a calibration curve, we prepared a set of standard samples in the same way using the corresponding oxides SrO, BaO, and Nb_2O_5 instead of SBN to cover a composition range of $x = 0.20 \ldots 0.85$.

In all measurements, the counting time was adjusted such that a number of total counts of approximately 10^6 was reached for each of the fluorescence lines. Thus the relative statistical error of the count rates was reduced to $\approx 10^{-3}$.

In order to reduce the influence of intensity fluctuations of the X-ray source, we define a relative strontium intensity as

$$I_{\mathrm{rel}} = \frac{N_{\mathrm{Sr}}}{N_{\mathrm{Sr}} + N_{\mathrm{Ba}}}, \tag{1}$$

where N are the count rates for the respective lines. These count rates are assumed to be proportional to the respective strontium or barium contents. For the relation, we use element-specific generalized factors Q containing all experimental conditions including source intensity, quantum yield and detector sensitivity for the specific line, spectrometer throughput, etc.

$$N_{\mathrm{Sr}} = Q_{\mathrm{Sr}} x, \qquad N_{\mathrm{Ba}} = Q_{\mathrm{Ba}}(1 - x). \tag{2}$$

Defining the ratio $R = Q_{\mathrm{Ba}}/Q_{\mathrm{Sr}}$, we arrive at

$$I_{\mathrm{rel}} = \frac{x}{x + R(1 - x)} \tag{3}$$

as a theoretical description for I_{rel}.

The values for the measured standards and the fitted calibration curve according to Eq. (3), using R as a fit parameter, are sketched in Fig. 3.

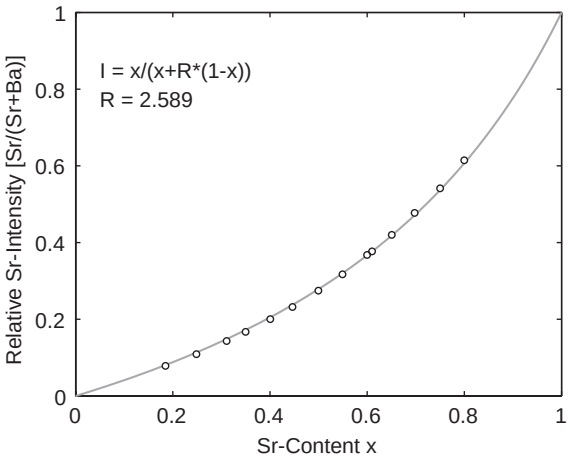

Fig. 3. Relative strontium intensity as described by Eq. (1) as a function of the strontium content (dots). The solid line represents a fit according to Eq. (3).

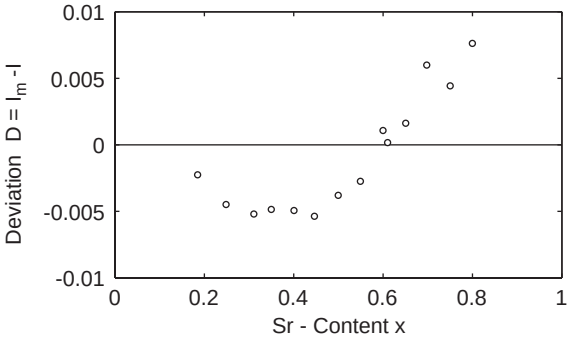

Fig. 4. Differences between the one-parameter fit and the measured relative strontium intensities.

The fit seems to be excellent, a closer inspection of the deviations as sketched in Fig. 4, however, shows a distinct systematic trend.

One could account for this trend *mathematically* by introducing a higher order correction into the fit, or *physically* by fixing a physical reason for the trend. We tried the latter as in the field of X-ray fluorescence analysis the deviations from linearity have been under discussion since nearly 60 years [15].

The main effects which have to be incorporated into a model calculation are absorption of the exciting radiation and reabsorption of the fluorescent radiation. Fig. 5 shows the relevant molar

absorbances [16] together with the energies of the fluorescence lines used.

Taking into account these absorption values and the compositions of the sample tablets, we calculated the absorption and emission depths for the two fluorescence lines used by appropriate numerical integrations. The results are shown in Fig. 6.

The calculations are done for two compositions, $x = 0.3$ and 0.7. A noticeable difference can only be found for the strontium Kα line, not for barium. Based on this fact, we included a reabsorption correction for the strontium count rate into the fit

$$I_{\mathrm{rel}}(x) = \frac{x(1 - A(1 - x))}{x(1 - A(1 - x)) + R(1 - x)}, \tag{4}$$

which introduces an additional reabsorption proportional to the barium content $1 - x$ with the proportionality A used as second fit parameter in addition to R. The deviations as documented in Fig. 7 are thus brought down to a merely statistical distribution.

Using the fit defined by Eq. (4), the crystal compositions for all crystals grown were determined.

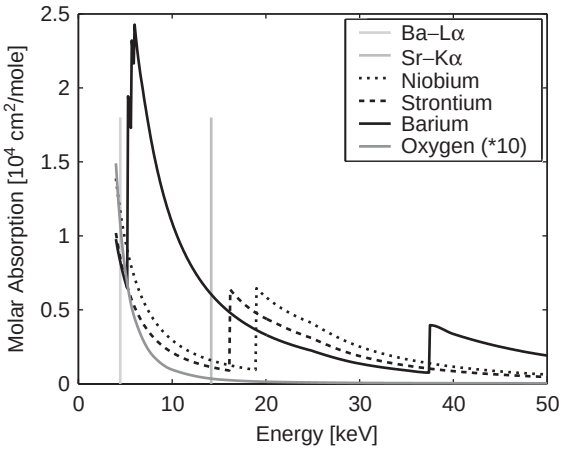

Fig. 5. Molar absorbances of the atoms mainly involved as a function of the X-ray energy and energy of the fluorescence lines used for the measurements.

4. Liquidus temperatures, phase diagram

For the determination of the phase diagram the liquidus temperatures were measured using a special furnace (Fig. 8). In this furnace tiny crystals were grown directly at a thermocouple from well-defined melts. The temperature of the melt was cycled in a small range around the melting temperature of the respective crystal. The exact melting temperature was then derived from the corresponding weight variations.

The solidus curve of the phase diagram is determined by the corresponding crystal compositions. These were measured as described in the previous section using large homogeneous single crystals grown from appropriate melts.

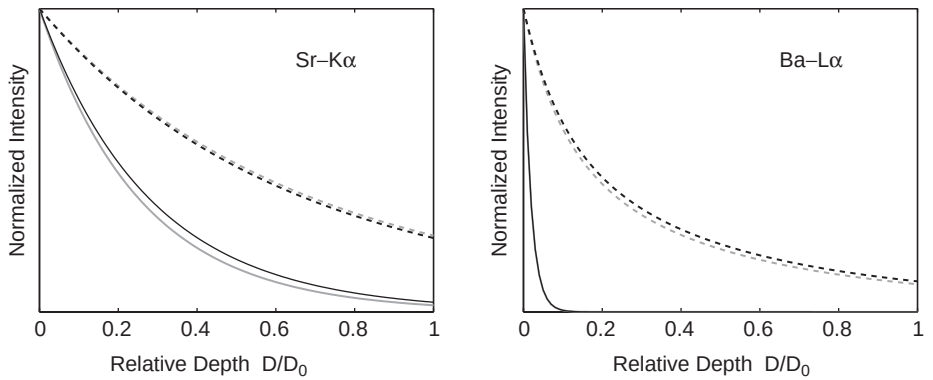

Fig. 6. Intensity profiles for the X-ray excitation of strontium and barium (dashed lines) and for the emission of the respective fluorescence energies (solid lines) as a function of the relative sample depth. Gray for a strontium content $x = 0.3$, black for $x = 0.7$.

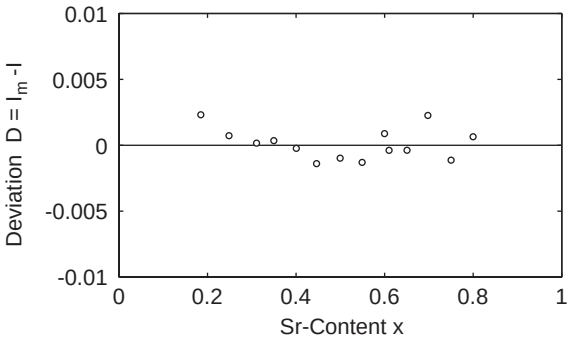

Fig. 7. Differences between the two-parameter fit—taking into account the reabsorption of the strontium fluorescence—and the measured relative strontium intensities. The deviation now is merely statistical.

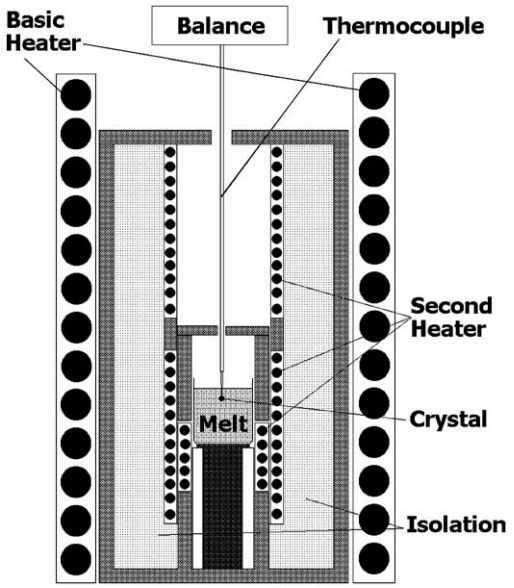

Fig. 8. Furnace utilized to measure the liquidus temperatures. Using a staggered heater concept, high-temperature accuracy could be achieved.

In addition to the liquidus and solidus curves in the existence region of the tetragonal tungsten–bronze structure, the liquidus temperatures in the strontium niobate range and in the barium niobate range have been measured. As no large crystals were grown there, only the melt compositions are determined. X-ray diffraction measurements on the small crystals grown in these two ranges, however, ensured that only pure barium niobate and pure strontium niobate, respectively, are crystallizing throughout these two side regions. Thus, we could determine the liquidus curves in these regions too. The temperatures of the eutectics are defined by the respective crossing points of the liquidus temperatures. The full phase diagram is depicted in Fig. 9. The solidus curves in the two border regions are omitted as no crystals were grown in these regions.

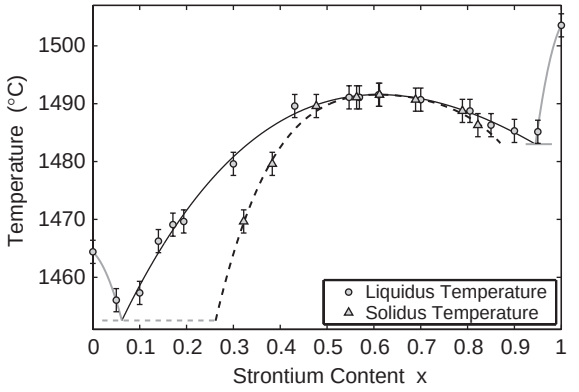

Fig. 9. Liquidus–solidus phase diagram of the solid solution barium niobate–strontium niobate. Measured data are indicated by dots with errorbars, full line (liquidus) and dashed line (solidus) are fits to the experimental data.

For the region, where SBN can be grown, the liquidus and solidus temperatures—T_L and T_S, respectively—can be described by two fourth-order polynomials as a function of the strontium content

$$T_L = (1441.3 + 196.50x - 247.70x^2 + 114.22x^3 - 24.023x^4)\ (^\circ\mathrm{C}), \quad (5)$$

$$T_S = (1247.1 + 1382.9x - 2968.9x^2 + 2893.7x^3 - 1091.0x^4)\ (^\circ\mathrm{C}). \quad (6)$$

From the phase diagram, the existence region of the tetragonal tungsten–bronze structure of SBN can be derived. The barium-rich limit lies at a strontium fraction x of 0.262—corresponding to a strontium fraction in the melt of 0.062, the strontium-rich limit at a strontium fraction of 0.870—corresponding to a strontium fraction in the melt of 0.945.

Eqs. (5) and (6), furthermore, allow to derive mutually corresponding melt and crystal compositions, x_m and x_c, respectively, resulting in the following functional relation for the crystal composition as a function of the melt composition

$$x_c(x_m) = 0.216 + 0.769x_m - 1.494x_m^2 + 3.282x_m^3 - 1.894x_m^4 \quad \text{for } 0.062 < x_m < 0.945. \quad (7)$$

5. Conclusion

Growing a series of strontium barium niobate crystals, $Sr_xBa_{1-x}Nb_2O_6$, with strontium contents x between 0.32 and 0.82 and measuring liquidus temperatures and crystal compositions, we could determine an accurate liquidus–solidus phase diagram for the system barium niobate–strontium niobate. The existence region for the tetragonal tungsten bronze structure of strontium barium niobate is found to be $0.26 < x < 0.87$. Melt temperatures span from 1452 °C for the barium side eutectic via 1492 °C for the congruently melting composition to 1483 °C for the strontium side eutectic.

References

[1] A.M. Glass, J. Appl. Phys. 40 (1969) 4699.
[2] F. Kahmann, J. Hohne, R. Pankrath, R.A. Rupp, Phys. Rev. B 50 (1994) 2474.
[3] R.R. Neurgaonkar, M.H. Kalisher, T.C. Lim, E.J. Staples, K.L. Keester, Mater. Res. Bull. 15 (1980) 1235.
[4] H.Y. Zhang, X.H. He, Y.H. Shih, L. Yan, J. Mod. Opt. 669 (1994) 6613.
[5] M. Wesner, C. Herden, R. Pankrath, D. Kip, P. Moretti, Phys. Rev. E 6403 (2001) 6613.
[6] A.S. Kewitsch, M. Segev, A. Yariv, G.J. Salamo, T.W. Towe, E.J. Sharp, R.R. Neurgaonkar, Appl. Phys. Lett. 64 (1994) 3068.
[7] R.R. Neurgaonkar, W.K. Cory, J.R. Oliver, E.J. Sharp, M.J. Miller, G.L. Wood, W.W. Clark III, A.G. Mott, G.J. Salamo, B.D. Monson, SPIE 1148 (1989) 2.
[8] A.A. Ballmann, H. Brown, J. Crystal Growth 1 (1967) 311.
[9] A.A. Ballmann, P.V. Lenzo, E.G. Spencer, Appl. Phys. Lett. 11 (1967) 23.
[10] P.B. Jamieson, S.C. Abrahams, Bernstein, J. Chem. Phys. 48 (1968) 5048.
[11] E.L. Venturini, E.G. Spencer, P.V. Lenzo, A.A. Ballmann, J. Appl. Phys. 39 (1968) 343.
[12] J.R. Carruthers, M. Grasso, J. Electrochem. Soc. 117 (1970) 1426.
[13] K. Megumi, N. Nagatsuma, Y. Kashiwada, Y. Furuhata, J. Mater. Sci. 11 (1976) 1583.
[14] R.R. Neurgaonkar, W.K. Cory, J.R. Oliver, E.J. Sharp, G.L. Wood, G.J. Salamo, Ferroelectrics 142 (1993) 167.
[15] J.P. Willis, G.R. Lachance, Rigaku J. 17 (2000) 23.
[16] See e.g. http://www.bmsc.washington.edu/scatter/.